Telescope alignment based on the sharpness function of under-sampled images

Min Li (李 敏)[1,2,3], Xin Liu (刘 鑫)[2], Ang Zhang (张 昂)[1,2,*], and Hao Xian (鲜 浩)[1,2,]**

[1]*Key Laboratory of Adaptive Optics, Chinese Academy of Sciences, Chengdu 610209, China*
[2]*Institute of Optics and Electronics, Chinese Academy of Sciences, Chengdu 610209, China*
[3]*University of Chinese Academy of Sciences, Beijing 100049, China*
**Corresponding author: zhangang@ioe.ac.cn; **corresponding author: xianhao@ioe.ac.cn*
Received October 6, 2018; accepted March 21, 2019; posted online May 31, 2019

The precise alignment of a high-performance telescope is a key factor to ensure the imaging quality. However, for telescopes with a wide field of view, the images are sometimes under-sampled. To study the effects of under-sampled images on the precision of telescope alignment, numerical simulations are implemented with the stochastic parallel gradient descent algorithm. The results show that the alignment program can converge stably and quickly. However, with the reduction of the full width at half-maximum of images, the relative residual errors increase from 9.5% to 19.5%, and the wavefront errors raise from 0.0972λ to 0.1074λ, indicating that the accuracy of the alignment decreases.

OCIS codes: 110.6770, 120.4820, 220.1140, 220.1080.
doi: 10.3788/COL201917.061101.

The alignment of telescopes is essential for their optimal performance[1]. For those with a small field of view (FOV) and undemanding image quality, one can correct only the on-axis field to achieve the best working state of telescopes, ignoring the effects of aberrations in the off-axis fields. But for telescopes with a wide FOV and a high requirement for image quality, when the on-axis field is aligned, the aberrations in the off-axis fields may be increased, such as coma and astigmatism[2]. As a result, the aberrations in both the on-axis and off-axis fields should be corrected.

There are many approaches for telescope alignment. All these methods can be classified into three categories. One is the direct wavefront sensor method (WFS)[3,4], which is most commonly used in the alignment of telescopes, such as the sensitive table method[5] and Shack–Hartmann wavefront sensor method[6]. This kind of method requires additional optical elements to measure the wavefront errors, increasing the complexity of optical systems. The second method is the image-based wavefront sensor method, for example, the phase retrieval (PR) method[7] and phase diversity (PD) method[8]. Compared with the WFS method, this kind of method only requires one or more detectors, without adding other optical components. However, it does entail more computation to estimate the wavefront errors. The third one is the image-based sharpness function method[9], which maximizes the sharpness function of images using an optimization algorithm to correct the misalignments. Compared with the other two kinds of approaches, this method only requires one detector placed in the focal plane to measure the sharpness of the images in real time, and the misalignments are corrected with the optimization algorithm. For the advantages of concise measurement systems and simple calculations, this method has been successfully used by Yang *et al.*[10] and Zhou *et al.*[11] to correct wavefront errors. In this Letter, we also use the sharpness function method to align the telescopes with a wide FOV. There are many sharpness functions that are commonly used for specific applications, such as the entire light intensity, partial intensity, and Strehl ratio. In this Letter, the root mean square radius (RMS) of images is employed as the merit function.

However, in imaging systems, especially for telescopes with a wide FOV, under-sampled images are common; nowhere is this problem more acute than on the Hubble Space Telescope (HST)[12]. Imperfect optics, finite detector arrays, and finite individual detector sizes all contribute to the non-ideal sampling of the scene information to meet the Nyquist criterion. The resulting images will be degraded by aliasing effects[13]. The under-sampled images addressed in this Letter are caused by finite individual detector sizes. The information missing from under-sampled images makes it difficult to detect faint sources and accurately represent the aberrations of spots. In the past few years, some research has been proposed[14,15]. All these methods are based on image reconstruction[16] to restore the information lost in under-sampled images. However, few efforts have been made to study the effects of under-sampled images on the accuracy of telescope alignment. This Letter focuses on this issue. The telescope is aligned using a stochastic parallel gradient descent (SPGD)[17] algorithm combined with the sharpness function of different sampling images. According to the Nyquist sampling condition, the largest sampling interval of detectors should be equal to or smaller than the optical cutoff period of the imaging system. Otherwise, the image will be under-sampled and aliasing will appear. Assuming the width of a CCD pixel is a (in μm), the minimum sampling frequency is calculated by the diagonal of the pixel, so the sampling frequency of the CCD is

$$v_s = \frac{1000}{a\sqrt{2}}\ \text{lp/mm} \Rightarrow v_N = \frac{v_s}{2} = \frac{500}{a\sqrt{2}}\ \text{lp/mm}, \tag{1}$$

where v_N represents the Nyquist frequency. According to the Rayleigh criterion, the resolution of a telescope with a circular aperture is defined as

$$\frac{\delta}{2} = \frac{1.22\lambda}{D} f_{\text{telescope}} = 1.22\lambda F^{\#}, \tag{2}$$

where δ is diameter of the Airy disk, λ is the central wavelength of the optical system, D is the aperture of the telescope, $f_{\text{telescope}}$ is the focal length, and $F^{\#}$ is F number. The maximum spatial frequency of the telescope is

$$v_{\max} = \frac{2}{\delta} = \frac{1}{1.22\lambda F^{\#}}. \tag{3}$$

According to the Nyquist sampling condition, the spatial frequency of the telescope imaging system should be equal to or smaller than half the detector spatial frequency:

$$v_{\max} \le v_s/2 \Rightarrow \delta \ge 4\sqrt{2}a. \tag{4}$$

Equation (4) means the diameter of the telescope spots should be larger than 4 pixels, otherwise the spots will be under-sampled.

In this Letter, both well-sampled and under-sampled images are simulated to correct the misalignments. The under-sampled images with various under-sampling factors are simulated by the down-sampling method. The larger the under-sampling factors are, the smaller the diameter of the images will be. The diameters of the images are calculated by the full width at half-maximum (FWHM). If the FWHM of the image is smaller than 4 pixels, it is an under-sampled image. The telescope used in this Letter is a Cassegrain system with a full FOV of 0.7° and a central wavelength of 0.65 μm. The other parameters are shown in Table 1.

Table 1 shows that the primary mirror (PM) of the Cassegrain telescope was a parabolic reflector with a conic of −1, semidiameter of 880 mm, and radius of −5400 mm. The distance between the primary and secondary mirror was −2292 mm. The secondary mirror (SM) was a hyperbolic reflector with a conic of −1.688, semidiameter of 142.9 mm, and radius of −938 mm. There are some other optical elements used to correct the field curvature. The telescope system is shown in Fig. 1.

Table 1. Parameters of the Cassegrain Telescope System

Surface	Semidiameter (mm)	Radius (mm)	Thickness (mm)	Conic
PM	880	−5400	−2292	−1
SM	142.9	−938	1807	−1.688

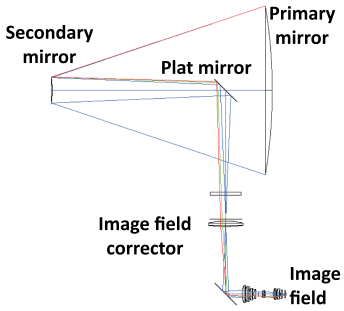

Fig. 1. Cassegrain telescope system.

For a Cassegrain telescope, the spherical aberration is corrected. However, the coma term grows quickly when the FOV is far away from the optical axis. As a result, aberrations in both the on-axis and off-axis fields should be corrected. In this Letter, the telescope is aligned based on three fields of images, including the on-axis field, which is also called 0field and two off-axis fields. The normalized field point coordinates were 0field (0°, 0°), 0.8field (0°, −0.28°), and 1field (−0.35°, 0°).

For large aperture telescope systems, we set the primary mirror as a reference that is being fixed in place. The misalignments of the secondary mirror related to the primary mirror consist of six degrees of freedom, including decentration along the x, y, z axes and tilt/tip about three axes. The rotation about the z axis, which is also the optical axis, has no effect on the quality of images, so it is usually ignored. As a result, the secondary mirror has five degrees of freedom related to the primary mirror, including decentration along the z axis (D_z), decentration along the x and y axes (D_x, D_y), and tilt about the x and y axes (T_x, T_y). To verify the effect of the alignment method, large misalignment errors were given. The misalignments corresponding to five degrees of freedom are shown in Table 2.

The decentrations along the x axis (D_x) and y axis (D_y) are 600 μm and 880 μm, respectively. The decentration along the z axis (D_z) is 80 μm. The tilts about the x (T_x) and y (T_y) axes are 0.1° and 0.03°, respectively.

In this Letter, the telescope system is aligned using the SPGD algorithm, which is a model-free iteration control method. The iterative formula of the SPGD algorithm is[18]

$$u^{k+1} = u^k - \gamma \delta J^k \delta u^k, \tag{5}$$

where k is the number of iterations. u is the control variable, composed of five degrees of freedom of the secondary mirror. γ is the gain coefficient. δJ is the variation of merit function.

Table 2. Misalignment Errors of the Secondary Mirror

D_x (μm)	D_y (μm)	D_z (μm)	T_x (°)	T_y (°)
600	880	80	0.1	0.03

The sharpness function used in this Letter is the RMS of the images, defined as[19]

$$J = \frac{\iint \sqrt{(x-x_0)^2+(y-y_0)^2}\, I(x,y)\mathrm{d}x\mathrm{d}y}{\iint I(x,y)\mathrm{d}x\mathrm{d}y}, \qquad (6)$$

where (x_0, y_0) is the centroid of the light intensity distribution, and (x, y) is the distribution coordinates of the CCD. $I(x, y)$ is the light intensity on the pixel whose coordinate is (x, y) in the focal plane.

The alignment of the telescope can be divided into two parts. The first step is the on-axis field correction, in which the RMS of the far-field image is employed as the sharpness function to compensate the spherical aberrations. The second step is the all fields correction, including both the on-axis and off-axis fields to compensate the spherical aberrations, coma, and astigmatism simultaneously. In this part, the RMSs of both the on-axis and off-axis field images are calculated, and the average value of the RMSs is used as the sharpness function. The telescope alignment process based on the sharpness of images with the SPGD method is shown in Fig. 2.

The designed images corresponding to different fields that are obtained when the telescope is in designed working conditions and the misaligned images obtained in misaligned working conditions are shown as Fig. 3.

Figure 3(a) shows designed images, the on-axis field of which is almost a perfect Airy spot, while the off-axis designed images carry a few aberrations, including coma and astigmatism. Figure 3(b) shows the misaligned images bringing large aberrations in both the on-axis and off-axis fields. J is the RMS of the image spots. We have known that when the FWHM is smaller than 4 pixels, the images are under-sampled. With the increase of FWHMs, the information carried by the images becomes richer and

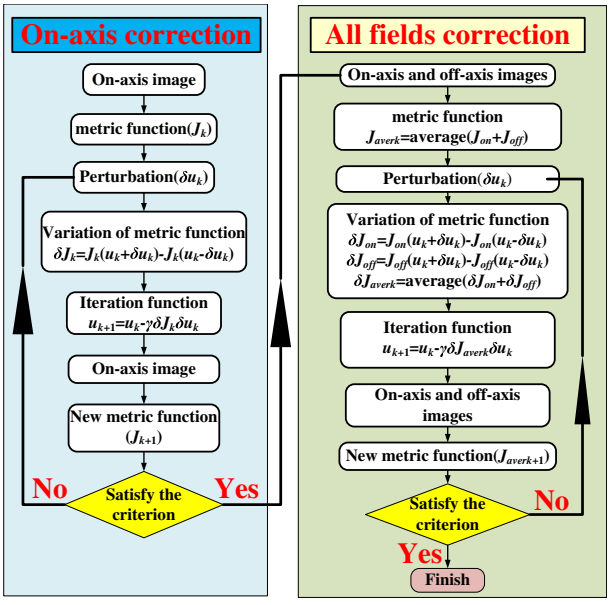

Fig. 2. Process of telescope alignment.

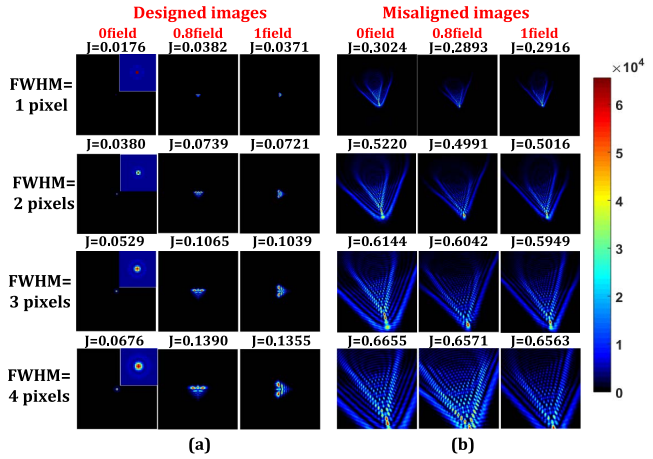

Fig. 3. Designed and misaligned images with different FWHMs. (a) Designed images. (b) Misaligned images.

the size of the spots becomes larger, as do the RMSs of images. That is because all the images have the same size of 200 pixels × 200 pixels. The more information the images bring, the larger the RMS will be. To analyze the aliasing effects of under-sampling, the spectra of the 0field designed images are calculated and shown in Fig. 4.

Figure 4 shows the spectrum of the 0field designed images. We can see that with the decreases of FWHM, aliasing appears and becomes more serious. When the FWHM of the image is 1 pixel, the aliasing becomes more obvious with high frequency adding to the low frequency. In addition, the information is seriously lost and the images cannot display the aberrations accurately, which may decrease the accuracy of the alignment.

The telescope is aligned based on both the well-sampled and different under-sampled images. In the alignment processes, the step sizes are same with $\delta u = [0.2\ \mathrm{mm}, 0.2\ \mathrm{mm}, 0.1\ \mathrm{mm}, 0.02°, 0.02°]$, while the gain coefficients γ of the program are different for under-sampled and well-sampled images. For under-sampled images with FWHM as 1 and 2 pixels, the gain coefficient is 5, while for images

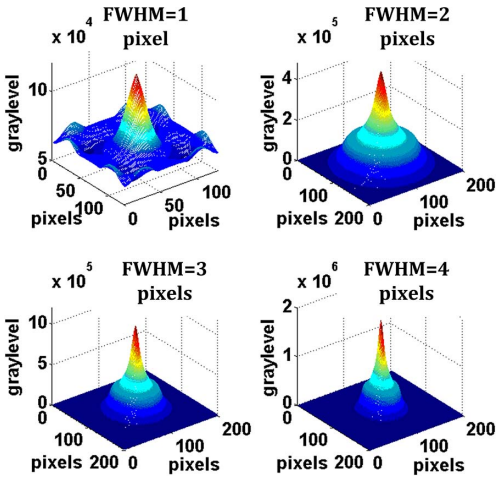

Fig. 4. Spectrum of the 0field designed image with FWHMs of 1, 2, 3, and 4 pixels.

with FWHM as 3 pixels, the gain coefficient is 3, and for images with FWHM as 4 pixels, the gain coefficient is 1. The iteration number is set as 200. The results of the alignment are shown in Fig. 5.

According to Fig. 5, the images after correction have similar shapes even though the FWHMs of the spots are different. The images in the off-axis fields after on-axis correction still bring coma and astigmatism aberrations because when the on-axis aberrations are aligned the aberrations in the off-axis fields still exist. After the all fields correction, aberrations in both the on-axis and off-axis fields are well corrected, and the shapes of the images are similar with the designed ones. The 0 field images after correction are almost Airy disks, indicating that the misalignments are well corrected.

The changes of the RMS of the image spots during the correction process are shown in Fig. 6.

Figures 5 and 6 show that whether the images are well-sampled or under-sampled, and the alignment processes converge stably and quickly. With the reduction of the FWHM, the RMS decreases. That is because all the images have the same size of 200 pixels × 200 pixels, so with the reduction of the FWHM the information carried by images is decreased. So the RMS of the under-sampled images becomes smaller.

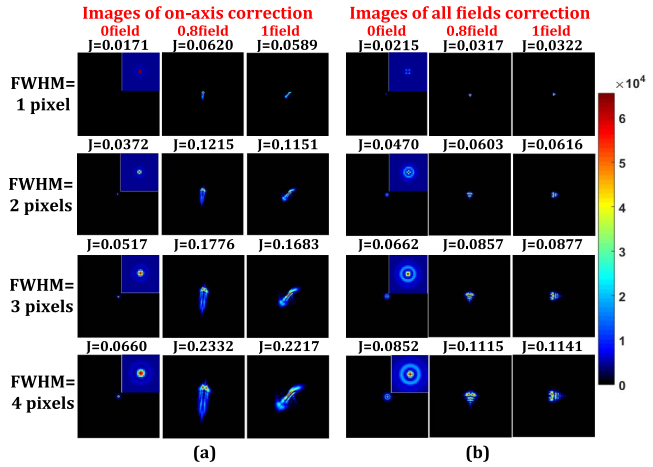

Fig. 5. Results of the telescope alignment. (a) Results of the on-axis correction. (b) Results of the all-fields correction.

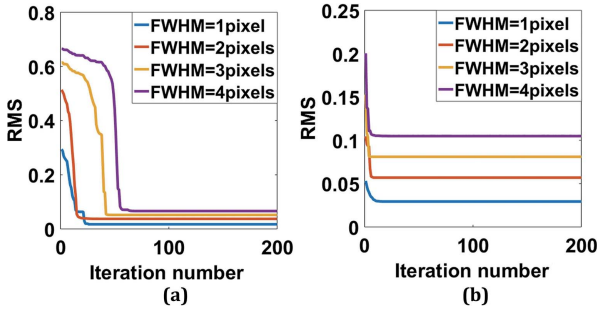

Fig. 6. Convergence curves of RMS during the correction. (a) RMS changes during the on-axis field correction. (b) RMS changes during the all-fields correction.

Table 3. Residual Errors and Wavefront Residual Errors of Optical System Measured After Correction

FWHM(pixel)		1	2	3	4
Residual errors	D_x (mm)	0.030	0.051	0.030	0.023
	D_y (mm)	−0.276	−0.226	−0.133	−0.098
	Dz (mm)	0.008	0.008	0.008	0.008
	T_x (°)	0.038	0.031	0.018	0.013
	T_y (°)	0.004	0.007	0.004	0.003
RRE (%)		19.5	19.7	12.3	9.5
WRE (λ)		0.1074	0.1071	0.1014	0.0972

To verify the accuracy of the alignments based on both the well-sampled and under-sampled images, the residual errors and the wavefront residual errors (WREs) after correction are calculated. The results are shown in Table 3.

Table 3 shows the residual errors of the misalignments, which are calculated by the difference between the designed positions and the actual positions of the secondary mirror after correction, reflecting the accuracy of the alignments. The relative residual errors (RREs) are defined as the mean ratios of the residual errors and the theoretical misalignments corresponding to different degrees of freedom. The results show that the RREs are increased with the decrease of the FWHMs, indicating that the accuracy of alignments becomes worse with the growth of under-sampled factors.

To verify the accuracy of alignment, WREs in the 0field are calculated using a Zernike polynomial before and after correction. The designed working condition of telescope has few aberrations with WREs of 0.0919λ. When the telescope is in the misaligned working condition, the system carries large aberrations with WREs of 3.1028λ. For different under-sampled factors, the 0field WREs after the alignment process are shown in Table 3. The results indicate that with the increase of FWHMs, the WREs decrease and are close to the designed working condition. For images with an FWHM of 4 pixels, the WRE is 0.0972λ, which is closest to the designed condition of 0.0919λ. Therefore, with the decreases of the FWHM, the WRE increases, reducing the accuracy of alignment. That is because the information of the images is more seriously lost when the under-sampled factor increases, so they cannot accurately express the aberrations of the optical system.

In conclusion, the misalignments of telescopes can be corrected by maximizing the sharpness function of the far-field images. Whether the images are well-sampled or under-sampled, the correction process can converge stably and rapidly, and the images after correction have similar shapes and sizes even when the FWHMs of the images are different. The accuracy of alignment is analyzed by the RREs and WREs. The RREs show that with the reduction of the FWHM, the accuracy of alignment becomes

worse, increasing from 9.5% to 19.5%, and the WREs increase from 0.0972λ to 0.1074λ, indicating that the undersampled images decrease the accuracy of alignment and cannot express the aberrations exactly because much information is lost. So, for future work, when the telescopes are aligned based on the sharpness function of far-field images with a different sampling frequency, two possible methods can help improve the precision of alignment. One is to find a new merit function that has no relation to the sampling of images; the other is to reconstruct the undersampled images to recover the lost information.

This work was supported by the National Natural Science Foundation of China (No. 11873008).

References

1. E. Luna, A. Cordero, J. Valdez, L. Gutiérrez, and L. Salas, Publ. Astron. Soc, Pac. **111**, 104 (1999).
2. H. S. Yang, Y. W. Lee, E. D. Kim, Y. W. Choi, Ad. Aziz, and Ad. Rasheed, Proc. SPIE **5528**, 334 (2004).
3. S. Q. Wang, K. Wei, W. J. Zheng, and C. H. Rao, Chin. Opt. Lett. **14**, 100101 (2016).
4. Z. L. Xie, H. T. Ma, B. Qi, G. Ren, J. Shi, X. He, Y. Tan, L. Dong, and Z. Wang, Chin. Opt. Lett. **15**, 041101 (2017).
5. J. W. Figoski, T. E. Shrode, and G. F. Moore, Proc. SPIE **1049**, 166 (1989).
6. S. Kim, H. S. Yang, Y. W. Lee, and S. W. Kim, Opt. Express **15**, 5059 (2007).
7. R. Gerchberg and W. Saxton, Optik **35**, 275 (1971).
8. M. Bolcar and J. Fienup, Appl. Opt. **48**, A5 (2009).
9. J. R. Fienup and J. J. Miller, J. Opt. Soc. Am. **20**, 609 (2003).
10. H. Z. Yang, X. Y. Li, and W. H. Jiang, Optica Acta **27**, 1356 (2007).
11. L. F. Zhou, A. Zhang, J. B. Zhang, X. L. Fan, L. Wei, S. Q. Chen, and H. Xian, Acta Phys. Sin. **65**, 139501 (2016).
12. J. C. Gillette, T. M. Stadtmiller, and R. C. Hardie, Opt. Eng. **34**, 3130 (1995).
13. A. S. Fruchter and R. N. Hook, Publ. Astron. Soc. Pac. **114**, 144 (2002).
14. L. D. Grey, Proc. SPIE **628**, 443 (1986).
15. J. C. Gillette, T. M. Stadtmiller, and R. C. Hardie, Opt. Eng. **34**, 3130 (1995).
16. C. T. Seo, S. W. Kang, and M. J. Cho, Chin. Opt. Lett. **15**, 081102 (2017).
17. H. Yang, X. Li, C. Gong, and W. Jiang, Opt. Express **17**, 3052 (2009).
18. X. L. Wang, P. Zhou, Y. X. Ma, J. Y. Leng, X. J. Xu, and Z. J. Liu, Opt. Lett. **36**, 3121 (2011).
19. C. Geng, W. Luo, Y. Tan, H. M. Liu, J. B. Mu, and X. Y. Li, Opt. Express **21**, 25045 (2013).